Research Square

Preprints are preliminary reports that have not undergone peer review.
They should not be considered conclusive, used to inform clinical practice,
or referenced by the media as validated information.

A Wireless Microrobot for Deep Brain Navigation at the Human Head Scale

Tian Qiu

tian.qiu@dkfz.de

German Cancer Research Centre (DKFZ) https://orcid.org/0000-0003-0932-5605

Meng Zhang

German Cancer Research Centre (DKFZ)

Jyothi Mariyanna

German Cancer Research Centre (DKFZ)

Moonkwang Jeong

German Cancer Research Centre (DKFZ) https://orcid.org/0000-0003-3731-1833

Andre Sagerer

Medical Faculty and University Hospital Carl Gustav Carus, TUD Dresden University of Technology, Dresden

Jiyuan Tian

German Cancer Research Centre (DKFZ) https://orcid.org/0009-0003-4467-3776

Yue Gao

German Cancer Research Centre (DKFZ) https://orcid.org/0000-0002-3613-1980

Rudi Apolle

National Center for Tumour Diseases (NCT) Dresden

Haoying Wang

German Cancer Research Centre (DKFZ)

Ann-Sophia Müller

German Cancer Research Centre (DKFZ)

Liyuan Tan

German Cancer Research Centre (DKFZ)

Rayan Younis

University Hospital Carl Gustav Carus Dresden https://orcid.org/0000-0002-7558-8043

Martin Wagner

University Hospital Carl Gustav Carus Dresden https://orcid.org/0000-0002-9831-9110

Tirosh Mekler

Technion – Israel Institute of Technology

Netanel Korin

Technion – Israel Institute of Technology https://orcid.org/0000-0001-7244-889X

Konstantin Morozov
Technion – Israel Institute of Technology
Alexander Leshansky
Technion – Israel Institute of Technology
Tareq Juratli
University Hospital Carl Gustav Carus Dresden

Article

Keywords:

Posted Date: November 9th, 2026

DOI: https://doi.org/10.21203/rs.3.rs-11230753/v1

License: This work is licensed under a Creative Commons Attribution 4.0 International License.
Read Full License

Additional Declarations: Yes there is potential Competing Interest. Meng Zhang and Tian Qiu have a pending patent on the device for propulsion in viscoelastic materials (EP25202803). The other authors declare no competing interests.

A Wireless Microrobot for Deep Brain Navigation at the Human Head Scale

Meng Zhang[1#], Jyothi Kumari Mariyanna[1,2#], Moonkwang Jeong[1#], André Sagerer[3], Jiyuan Tian[1], Yue Gao[1], Rudi Apolle[4], Haoying Wang[1], Ann-Sophia Müller[1,5], Liyuan Tan[1,6], Ryan Younis[7,8], Martin Wagner[7,8], Tirosh Mekler[9], Netanel Korin[9,10], Konstantin I. Morozov[11], Alexander M. Leshansky[11], Tareq Juratli[2,3,12], Tian Qiu[1,2,6*]

Affiliations

[1]Division of Smart Technologies for Tumour Therapy, German Cancer Research Centre (DKFZ), Dresden, 01307, Germany.
[2]Faculty of Medicine, Dresden University of Technology (TUD), Dresden, 01307, Germany.
[3]Department of Neurosurgery, University Hospital Carl Gustav Carus, Dresden, 01307, Germany.
[4]Department of Translational Imaging in Oncology, National Center for Tumour Diseases (NCT), NCT/UCC Dresden, a Partnership Between DKFZ, Faculty of Medicine and University Hospital Carl Gustav Carus, Dresden University of Technology, and Helmholtz-Zentrum Dresden-Rossendorf, Dresden, 01307, Germany.
[5]Faculty of Computer Science, Dresden University of Technology (TUD), Dresden, 01187, Germany.
[6]Faculty of Electrical and Computer Engineering, Dresden University of Technology (TUD), Dresden, 01307, Germany.
[7]Department of Visceral, Thoracic and Vascular Surgery, Faculty of Medicine and University Hospital Carl Gustav Carus, Dresden University of Technology (TUD), Dresden, 01307, Germany.
[8]Centre for the Tactile Internet with Human-in-the-Loop (CeTI), Dresden University of Technology (TUD), Dresden, 01062, Germany.
[9]Department of Biomedical Engineering, Technion – Israel Institute of Technology, Haifa, 32000, Israel.
[10]Fischell Department of Bioengineering, University of Maryland, College Park, MD 20742, United States.
[11]Wolfson Department of Chemical Engineering, Technion – Israel Institute of Technology, Haifa, 32000, Israel.
[12]National Centre for Tumour Diseases (NCT/UCC), Dresden, 01307, Germany.
[#]These authors contributed equally to this work.
[*]Corresponding author: tian.qiu@dkfz.de;

Abstract

Deep-brain interventions for neurological disorders—including biopsies, localized therapies, and neuromodulation—are fundamentally constrained by rigid, linear tools that limit manoeuvrability and increase tissue trauma. Here, we present BrainBot, a wireless magnetic microrobot capable of sustained, steerable propulsion through dense viscoelastic brain tissue at a human-head-relevant scale. BrainBot features a multithread helical geometry and thread-clearing microstructures that actively prevent tissue adhesion, enabling sustained, low-damage propulsion across an entire porcine brain and *ex vivo* human glioblastoma tissue. Using a magnetic navigation system with a 24 cm aperture, BrainBot achieves fluoroscopy-guided access to deep targets through dense brain parenchyma within an intact porcine head.

Furthermore, we demonstrate precise tissue sampling for spatially resolved genomics, deployment of optical fibres and electrical microwires, and localized drug delivery followed by post-retrieval MRI payload visualization. BrainBot establishes a minimally invasive platform for deep-brain navigation, opening new avenues for precision neurosurgical interventions.

Main text

Introduction

Access to deep brain regions is essential for both fundamental neuroscience and the diagnosis and treatment of neurological disorders. Tissue biopsy, neural recording and stimulation, and localized therapy require instruments or therapeutic agents to reach targets embedded within brain parenchyma. Clinical devices used in stereotactic procedures commonly have millimetre-scale outer diameters, approximately 1.8–2.5 mm for brain biopsy needles[1–3] and 0.9–1.5 mm for deep brain stimulation electrodes[4,5]. Their placement typically relies on rigid insertion shafts or supporting structures[6,7], and conventional rigid instruments follow straight trajectories[8] that restrict the routes available to avoid critical anatomy[4,7]. A device with a submillimetre diameter that generates propulsion locally and can be steered within tissue could expand access to deep targets while reducing the cross-sectional footprint of the penetrating instrument. Magnetically actuated microrobots offer remote control of miniature devices[9,10] for targeted delivery[11], tissue sampling[12] and localized intervention[13,14]. Recent platforms have integrated catheter deployment, magnetic navigation, fluoroscopic tracking and drug release within workspaces that accommodate human anatomy[9]. For intracranial applications, the microrobots are often operated in the cerebrospinal fluid or on the brain's surface where the resistance is relatively low[15]. Viscoelastic soft tissues, however, present a much harder obstacle to be penetrated by miniature robots. Such access requires a robot to penetrate a continuous viscoelastic tissue matrix while maintaining propulsion and directional control.

Progress towards tissue-penetrating robots has established several complementary approaches. Early studies demonstrated magnetic helical propulsion through bovine and porcine muscle using devices several millimetres in diameter[16,17]. At smaller scales, we previously showed that helical nanorobots can penetrate the vitreous body of the eye[18], and that a submillimetre helical robot with an optimized propeller geometry can move through mouse liver[19]. Direct navigation through brain tissue has also been demonstrated. Son *et al.* used a permanent-magnet array with a 6 cm bore to generate strong magnetic gradients and guide millirobots along curved paths through *ex vivo* porcine brain[20]. More recently, Ligtenberg *et al.* demonstrated helical propulsion (~2 mm in diameter and ~7 mm in length) and reverse locomotion in *ex vivo* ovine brain, including a perfused model, and developed an empirical framework for predicting magnetic step-out[21]. These studies establish the feasibility of intratissue locomotion and identify important constraints imposed by tissue mechanics and magnetic actuation. Despite these advances, sustained propulsion over centimetre-scale distances through brain parenchyma remains challenging for microrobots with submillimetre diameters. Extending their reach requires effective propulsion and steering throughout tissue traversal, together with

magnetic actuation in a system that accommodates human anatomy. Combining these capabilities with tissue sampling, payload deployment and retrieval would provide a basis for microrobotic intervention at deep brain targets.

Here, for the first time, we present BrainBot, a magnetically actuated microrobot for deep brain access at the scale of a human head. Deployed through a single cranial burr hole, BrainBot navigates brain tissue to reach deep-seated tumours for targeted tissue biopsy and localized drug delivery (Fig. 1). Its multithread helical body has an outer diameter of 594 μm and incorporates thread-clearing (TC) microstructures around an encapsulated, diametrically magnetized permanent magnet. A rotating magnetic field drives the rotation of the helix, which converts the rotation into tissue-penetrating propulsion (Supplementary Video 1). The actuation system generates ~14 mT at the centre of a 24 cm gantry aperture designed to accommodate a human head. During helical propulsion, displaced tissue can accumulate within the helical grooves and form a co-rotating plug[19], reducing the effective helicity of the robot–tissue interface and impairing thrust and forward motion (see adhered tissue around the robot in Fig. 2). To overcome this limitation, TC microstructures act as ramps that redirect entrained tissue radially out of the grooves during rotation. Particle tracking and numerical modelling elucidate the underlying tissue clearing mechanism. In brain-mimicking gel phantoms, TC structures enable clearance of up to 94% of surface-associated tracer particles after propulsion over one body length; in *ex vivo* porcine brain, they reduce tissue retention, sustain propulsion and increase penetration depth threefold relative to the robots without TC structures. It enables the traversal of an entire *ex vivo* porcine brain along a 6.7 cm path through grey and white matter (Supplementary Fig. 1) and can reach ~80% of the total cross-sectional depth beneath the brain surface within an *ex vivo* porcine head under fluoroscopic guidance. We further demonstrate biopsy at multiple locations in a resected human glioblastoma (GBM) specimen for spatially resolved genomic analysis, deployment of an optical fibre and an electrical microwire, and targeted delivery of a model drug. Following drug delivery, the robot is retrieved, permitting postoperative magnetic resonance imaging (MRI) of the brain. Together, these results establish a wireless microrobotic platform for active, long-range penetration of viscoelastic brain tissue, opening new avenues for minimally invasive deep-brain access, spatially resolved sampling, and localized payload delivery.

Results

The shape design of the BrainBot and thread-clearing mechanism

The propulsion module of BrainBot consists of three structural features: a custom tip, a helical thread, and embedded TC microstructures (Fig. 2a-2b). We fabricated the robot by two-photon polymerization, and optimized individual unit towards the goals of a large penetration depth and minimum surrounding tissue damage. The magnet core is selected as 380 μm in diameter for a sufficient magnetic moment to propel in a large working volume of a human head, and the outer diameter is 594 μm to minimize the damage to the brain tissue. A special-shaped two-pronged tip is designed to fracture brain tissue with large shear forces generated during the

rotation by the two eccentric sharp apices (Fig. 2b), which enhances forward propulsion velocity.

However, we observed the helical robot stalls after propelling in the brain tissue for a few millimetres. We found that a tissue plug (Fig. 2c and Supplementary Fig. 2) is formed around the helical structures, filling up the threads and rotating together with the robot. Due to the loss of the helical shape, the robot does not propel further. Thus, we invented TC structures (Fig. 2b), which embodies tapered slopes from the root of the thread to its outer profile to enable the tissue diverting mechanism—to push the tissue plug outward from the thread during the rotation of the robot. The weight of the adhered tissue is significantly decreased (Fig. 2d) after 10 min-propulsion in the porcine brain, which is 1.4 mg for robots without TC and 0.6 mg for robots with TC. The propulsion distance also significantly increases for more than 3 times (Fig. 2e): the robots without TC stall after ~6.7 mm (~2 Body Lengths, BL), whereas robots with TC consistently propel more than ~16.75 mm (~5 BL). Although the velocities of the robots without or with TC do not show significant difference in the first 10 s, the one without TC drops to almost zero at 300 s, whereas the one with TC keeps propelling at a fast speed (Fig. 2f). By performing microparticle tracking experiments in a transparent brain-mimicking gelatin phantom (details in Supplementary Note 1), we quantified the clearing efficiency of the TC structure. After the propulsion of one BL, the clearing percentage of all surface-adhered microparticles is only 55% on the robot without TC, whereas the percentage increases to 94% with TC (Supplementary Fig. 3 and Supplementary Video 2).

To demonstrate the tissue clearing mechanism, we performed Particle Tracking Velocimetry (PTV) on a simplified TC structure, a magnetically rotated cylinder with one groove in a brain-mimicking gelatin phantom (Fig. 2g-2l, Supplementary Note 2). Fluorescent particles mixed in the gel were imaged in the cross-sectional view and tracked to represent the motion of the gel. Fig. 2i,j show the tracked trajectory of representative particles under the robot frame, *i.e.* the angle of the robot is fixed and the surrounding medium, represented by the particle trajectory, moves relative to the robot. In the design without TC, the tracked particle is almost static relative to the robot (Fig. 2i) with a constant radius and angle (Fig. 2k), suggesting that the groove is filled with a gel plug that firmly adheres to the robot and co-rotates at the same angular velocity (Supplementary Video 3 and Supplementary Fig. 4). On the contrary, in the design with TC (Fig. 2j, Supplementary Video 4 and Supplementary Fig. 5), the tracer particle initially co-rotates with the robot, but it is radially diverted by the TC ramp to the surrounding medium. The interaction between the surrounding medium causes a phase lag in its rotation relative to the robot's rotation (starting at 5 s in Fig. 2l), and the particle is eventually cleared out of the groove (showing the large angular displacement of the particle starting at 9 s in Fig. 2l).

Computational fluid dynamics (CFD) simulation using a simplified yield stress fluid model with shear thinning behaviour (rheological data in Supplementary Fig. 6 and 7a and Supplementary Note 3) shows similar results, matching the observations in the PTV (Supplementary Fig. 7b). In the structure without the TC, a layer of unyielded medium co-rotates with the robot surface; With the TC, a larger yielded region is observed near the robot

surface, and a low-viscosity region develops at the tip of the TC and extends outward as a cone-shaped envelope. The fluid is pushed out of the groove in front of the TC and drawn into the groove at the rear of the TC (Supplementary Fig. 7c). The mass flow rate through the circumferential surface of the groove is increased an order-of-magnitude with the TC, comparing with that without the TC (Supplementary Fig. 7d). Combined experimental observations and theoretical modelling reveal that the TC structure generates localized high shear stress in the adhered co-rotating plug, inducing radial flow and interaction with the surrounding stationary medium. This relative motion between the plug and the robot clears the thread groove, allowing the helical geometry to be maintained and enabling sustained propulsion in viscoelastic tissues.

By measuring the propulsion velocity in the porcine brain, we further optimized the geometric and driving parameters of the BrainBot, including the pitch, the total length and the rotational frequency (methods in Supplementary Note 4 and Supplementary Fig. 8). As the results shown in Supplementary Fig. 9-10, the maximal velocity occurs with an optimal pitch of 125 μm. Increasing the robot length from 1 mm to 3 mm results in enhanced velocity. However, this improvement is accompanied by an increased minimum turning radius (Supplementary Fig. 11), indicating a trade-off between propulsion speed and manoeuvrability. In brain tissue, the optimal driving frequency is ~2 Hz, where the robot reaches a maximum velocity of 0.04 ± 0.01 mm s^{-1} (Fig. 2m) and a maximum stall force of 3.49 ± 0.42 mN (Fig. 2n, methods in Supplementary Note 5).

3D Navigation of the BrainBot

We demonstrated BrainBot's wireless actuation and navigation capabilities in a transparent gelatin phantom (Supplementary Note 6). The robot was actuated to follow a pre-defined trajectory of the letter 'N' in the horizontal plane, and subsequently transitioned to the vertical plane to trace the letter 'T' (Fig. 2o, Supplementary Video 5). The procedure used a custom 3D magnetic navigation system (MANAS) with a 24 cm-gantry aperture, which is designed to fit a porcine head (Supplementary Fig. 12) and has the potential to accommodate an average human skull (~18.2 cm in length and ~14.1 cm in width [22]). MANAS enables wireless actuation and navigation of the BrainBot within a workspace of approximately ~7×7×7 cm^3 (Fig. 2p, details of the experimental setup are shown in Supplementary Fig. 13 and Supplementary Note 7).

To fully characterize the ability of propulsion and steering, we performed the test of robot propulsion in *ex vivo* porcine brain under ultrasound imaging. BrainBot can penetrate an entire porcine brain with a path length of ~6.7 cm. It was inserted in the frontal-lobe grey matter, navigated across the white matter, passed the parietal lobe, and exited near the occipital lobe (Supplementary Fig. 1 and Supplementary Video 6). To our knowledge, it achieves the longest continuous path of a micro-sized robot in soft brain tissues reported to date. Ultrasound imaging revealed a linear hyperechoic structure (0.3 mm in diameter and 10 mm in length) in the way of the robot. BrainBot was steered to avoid it under live ultrasound guidance. Then, the robot was retrieved by reversing the actuation direction and adjusting the field orientation to trace

the insertion path at the entry point in 9 min (Supplementary Fig. 14 and Supplementary Video 7). The forward linear velocity along the curved path is 0.06 mm s^{-1} on average and the backward velocity is 0.10 mm s^{-1}, both with a rotational frequency of 2 Hz.

Human GBM tissue sampling by BrainBots for molecular diagnostics

Functional modules for biomedical applications can be selectively integrated with the propulsion module on BrainBots. The biopsy module uses a 3D-printed needle tip as an integrated biopsy cavity located at the rear of the robot to retrieve GBM tissue for molecular diagnostics. This enables controlled tissue sampling precisely when the robot reverses its propulsion from forward to backward. A scanning electron microscopy (SEM) image (Fig. 3a) shows the biopsy needle tip with frangible structures at both the junction with the robot body and along the needle shaft. Four venting holes located near the connection point facilitate the expulsion of trapped liquid during tissue excision, thereby relieving internal pressure and improving biopsy sample collection efficiency. As a proof-of-concept demonstration, we performed robot-assisted *ex vivo* biopsies in porcine brains. To create a localized contrast-enhanced region as the biopsy target, a labelling solution (5 μL of 1 mg mL^{-1} methylene blue) was injected into the porcine brain (outlined by the green dashed line in Supplementary Fig. 15). The biopsy robot was then navigated to the target site. Upon reaching the target, the robot initiated reverse rotation to perform precise tissue excision. Video analysis confirmed a targeting accuracy of ~0.7 mm. Once the biopsy cavity was filled, the robot navigated back along the entry trajectory, minimizing tissue damage and enabling full retrieval for downstream analysis (*e.g.*, MRI). Methylene blue staining in the harvested tissue verified spatial targeting by the BrainBot (Fig. 3b). The biopsy yielded ~0.52 mg of tissue on average, calculated by subtracting the mass of tissue adhered to control robots without the biopsy cavity (0.66 mg) from the total mass gain of biopsy robots (1.18 mg; Fig. 3c,d), providing sufficient cells and DNA yields for downstream diagnostics (Supplementary Fig. 16). Ultrasound guidance enabled continuous monitoring throughout navigation, tissue sampling, and robot retrieval (Fig. 3e and Supplementary Video 8).

We successfully tested the BrainBot in an *ex vivo* human glioblastoma specimen measuring ~48 × 35 × 42 mm^3 (Fig. 3f). The *en bloc* resected tissue served as a model to evaluate robot transversal through pathological brain tissue, a challenging environment characterized by mechanical heterogeneity due to hypervascularization, intratumoral necrosis, and cellular debris. Ultrasound imaging identified hyperechoic vessel-like structures (hundreds of micrometres in diameter). Upon encountering these structures, the robot paused, suggesting insufficient penetration force and thereby preventing damage to larger vessels. The robot was subsequently steered around the vessel via an external magnetic field to continue its forward trajectory (Supplementary Video 9).

Four BrainBots were sent to four distinct sites in the GBM specimen (Fig. 3f) to take tissue mini-biopsy. Representative histological analysis (Fig. 3g) shows preserved cellular morphology and enough tissue for molecular testing. Subsequent sequencing of the biopsies was performed (Supplementary Note 8). All samples share the same set of polymorphisms, confirming their origin from a single patient. Mini-biopsies revealed highly concordant

genomic alterations as the control group, the formalin-fixed, paraffin-embedded (FFPE) tumour sample. Copy number variation (CNV) analysis demonstrated high-level EGFR amplification in all four mini-biopsies and CDKN2A/B deletion in three mini-biopsies, consistent with the control (Fig. 3h). Sequence variants in EGFR, NF1, PTEN and TERT promoter were identified in every sample. Despite overall similarity, TP53 splice-site disruptions were only detected at Positions 1 and 3, but not Positions 2 and 4, suggesting GBM intratumoural heterogeneity. These results highlight the BrainBot's potential for the biopsy of human GBM tissues and the mapping of spatial genomic diversity within tumours.

BrainBot further enables targeted delivery of tethered payloads, such as an optical fibre and an electrical wire, into brain tissue. Equipped with a 250-µm-diameter optical fibre, the robot utilizes a flat conical cap-and-socket joint to maintain secure rotor anchoring, while allowing unconstrained rotation to propel and drag the payload (Supplementary Fig. 17a-b). *Ex vivo* validation confirmed continuous functional delivery of an optical fibre, evidenced by green laser transmission at its distal tip (Supplementary Fig. 17c). Stable navigation throughout the delivery process was tracked via continuous ultrasound imaging (Supplementary Fig. 17d and Supplementary Video 10). Besides the optical fibre, BrainBot successfully transported a copper microwire for more than 25 mm in a gel phantom and executed the controlled release (Supplementary Video 11). *Ex vivo* testing confirmed full-cycle deployment of a 30-µm-diameter microwire in porcine brain tissue (Supplementary Video 12). Together, these results highlight the potential of BrainBot for the precise delivery and positioning of implantable neural devices, such as those required for optogenetics[23] and deep brain stimulation[24].

Safety assessment of the BrainBot

BrainBot's operational safety was confirmed through material biocompatibility assays and tissue integrity evaluations. Co-culture assays revealed 99% cell viability (Supplementary Fig. 18), confirmed by complete encapsulation of the internal magnet within a biocompatible shell using medical-grade glue. Histological examination of porcine brain tissue after BrainBot penetration showed minimal cytoarchitectural disruption along the trajectory measuring an average diameter of 535 ± 59 µm (Fig. 3i, Supplementary Figs. 19 and 20). For post-hoc trajectory analysis, a cotton thread (fibres marked by green triangles) was trailed behind the robot through the brain tissue to prevent tissue collapse. These results demonstrate that BrainBot enables effective tissue access and functional operations, while maintaining cell viability and minimizing tissue structural damage.

Targeted drug delivery of the BrainBot in a porcine head

Beyond diagnostic applications, BrainBot can also be applied for targeted drug delivery. To evaluate the wireless delivery setup in a clinically relevant environment, the MANAS was integrated with a C-arm X-ray imaging platform (Fig. 4a) to enable fluoroscopy-guided navigation inside a porcine head (Fig. 4b). The robot was inserted through a burr hole (Fig. 4c, blue arrow) at an initial entry angle of 25° relative to the vertical axis, re-oriented to 75° after advancing ~2 body lengths (BL) at 2.5 min, and subsequently adjusted to 45° at 4.5 min to travel an additional ~4 BL toward the planned target (Supplementary Video 13). CT imaging confirmed deep target reaching, showing the magnetic core as a hyperattenuating region 30

mm beneath the brain surface—corresponding to approximately 80% of the total cross-sectional depth (37.6 mm, Fig. 4d). Following navigation, BrainBot was retrieved by reversing its rotation direction to propel backward toward the brain surface, where it was collected using a small permanent magnet.

Finally, we evaluated the targeted delivery of a model drug and performed postoperative MRI—the clinical gold standard for GBM diagnosis and evaluation—to assess procedure-related tissue alterations and confirm safety. However, retaining the robot's permanent magnetic core in the brain during MRI would induce severe magnetic susceptibility artifacts[25]. To maintain MRI compatibility, we implemented a sequential workflow of targeted payload delivery followed by complete robot retrieval. SEM confirmed the micro-structured loading cavity located at the robot's anterior tip (Fig. 4e). To minimize premature diffusion during navigation, the loading chamber was filled with a solid cargo – a dried gelatin matrix impregnated with an MRI contrast agent as a model drug (Fig. 4f). Payload release was achieved via a mechanical push-release mechanism (Fig. 4g): the cargo remained encapsulated during forward propulsion, and detached during the retraction of the robot due to the relative motion of the body and the plunger (Supplementary Fig. 21 and Supplementary Video 14). Postoperative MRI scans revealed localized hyperintense foci corresponding to the deposited model drug, with no detectable magnetic susceptibility artifacts (Fig. 4h). These findings confirm both successful targeted payload delivery to discrete brain regions and complete robot retrieval.

Conclusion

In this work, we present BrainBot, a magnetic microrobot that enables sustained, steerable locomotion through deep brain tissue at the human head scale. Its thread-clearing microstructures redirect entrained tissue out of the helical grooves, limiting the formation of co-rotating plugs and preserving the mechanical engagement required to generate thrust. Particle tracking and numerical modelling elucidate the tissue clearing mechanism, while experiments in *ex vivo* porcine brain demonstrate reduced tissue retention and sustained penetration. These capabilities enable a sub-millimetre robot to traverse an entire *ex vivo* porcine brain along a 6.7 cm path through grey and white matter. Fluoroscopy-guided navigation within an *ex vivo* porcine head further demonstrates access to ~80% of the total cross-sectional depth beneath the brain surface using a magnetic actuation system designed to accommodate a human head. Targeted sampling of a resected human glioblastoma specimen enables spatially resolved genomic analysis, while optical fibre and electrical microwire deployments and localized drug delivery demonstrate complementary configurations for interventions. Together, these results establish tissue clearing as a design strategy for maintaining propulsive engagement during helical locomotion through soft tissues, connecting sustained penetration with functional operations for deep brain targets. BrainBot establishes a new class of minimally invasive, wireless neurosurgical tools capable of performing precise diagnostics and therapeutics deep within the brain.

References

1. Yuen, J. *et al.* A Sequential Comparison on the Risk of Haemorrhage with Different Sizes of Biopsy Needles for Stereotactic Brain Biopsy. *Stereotact. Funct. Neurosurg.* **92**, 160–169 (2014).
2. Vijian, K. *et al.* Improving Diagnostic Yield and Accuracy of Stereotactic Biopsies through Changes in Practice and Techniques: An 8-Year Single-Center Comparative Study. *Asian J. Neurosurg.* **19**, 701–706 (2024).
3. Meinert, F. *et al.* Accuracy of frameless stereotactic brain biopsy: a retrospective cohort study with MRI-only and MRI-CT fusion navigation. *Acta Neurochir. (Wien)* **167**, 327 (2025).
4. Thielen, B. & Meng, E. A comparison of insertion methods for surgical placement of penetrating neural interfaces. *J. Neural Eng.* **18**, 041003 (2021).
5. Ng, P. R., Bush, A., Vissani, M., McIntyre, C. C. & Richardson, R. M. Biophysical Principles and Computational Modeling of Deep Brain Stimulation. *Neuromodulation Technol. Neural Interface* **27**, 422–439 (2024).
6. Chapelle, F. *et al.* Early Deformation of Deep Brain Stimulation Electrodes Following Surgical Implantation: Intracranial, Brain, and Electrode Mechanics. *Front. Bioeng. Biotechnol.* **9**, 657875 (2021).
7. Huang, S. *et al.* Hybrid pneumatic-hydraulic actuation for MRI-guided robotic stereotactic neurointervention. *Sci. Adv.* **11**, eady3624 (2025).
8. Wang, X. *et al.* Intravascular delivery of an ultraflexible neural electrode array for recordings of cortical spiking activity. *Nat. Commun.* **15**, 9442 (2024).
9. Landers, F. C. *et al.* Clinically ready magnetic microrobots for targeted therapies. *Science* **390**, 710–715 (2025).
10. Medina-Sánchez, M. & Schmidt, O. G. Medical microbots need better imaging and control. *Nature* **545**, 406–408 (2017).
11. Nelson, B. J. & Pané, S. Delivering drugs with microrobots. *Science* **382**, 1120–1122 (2023).
12. Liu, W. *et al.* Untethered Microgrippers for Biopsy in the Upper Urinary Tract. *Adv. Healthc. Mater.* **13**, 2401407 (2024).

13. Chen, H. *et al.* Magnetic medical microrobots with memory-capable genetic circuits. *Sci. Adv.* **12**, eaeb2528 (2026).

14. Jeong, M., Tan, X., Fischer, F. & Qiu, T. A Convoy of Magnetic Millirobots Transports Endoscopic Instruments for Minimally-Invasive Surgery. *Adv. Sci.* **11**, 2308382 (2024).

15. Wang, B. *et al.* Magnetically driven biohybrid blood hydrogel fibres for personalized intracranial tumour therapy under fluoroscopic tracking. *Nat. Biomed. Eng.* **9**, 1471–1485 (2025).

16. Ishiyama, K., Sendoh, M., Yamazaki, A. & Arai, K. I. Swimming micro-machine driven by magnetic torque. *Sens. Actuators Phys.* **91**, 141–144 (2001).

17. Rahmer, J., Stehning, C. & Gleich, B. Remote magnetic actuation using a clinical scale system. *PLOS ONE* **13**, e0193546 (2018).

18. Wu, Z. *et al.* A swarm of slippery micropropellers penetrates the vitreous body of the eye. *Sci. Adv.* **4**, eaat4388 (2018).

19. Li, D., Jeong, M., Oren, E., Yu, T. & Qiu, T. A Helical Microrobot with an Optimized Propeller-Shape for Propulsion in Viscoelastic Biological Media. *Robotics* **8**, 87 (2019).

20. Son, D., Ugurlu, M. C. & Sitti, M. Permanent magnet array–driven navigation of wireless millirobots inside soft tissues. *Sci. Adv.* **7**, eabi8932 (2021).

21. Ligtenberg, L. W. *et al.* Performance Estimation and Ex Vivo Validation of Untethered Magnetic Robots in Soft Tissue. *Adv. Sci.* e77011 (2026) doi:10.1002/advs.77011.

22. Cotton, F. *et al.* Cranial sutures and craniometric points detected on MRI. *Surg. Radiol. Anat.* **27**, 64–70 (2005).

23. Deisseroth, K. Optogenetics: 10 years of microbial opsins in neuroscience. *Nat. Neurosci.* **18**, 1213–1225 (2015).

24. Krauss, J. K. *et al.* Technology of deep brain stimulation: current status and future directions. *Nat. Rev. Neurol.* **17**, 75–87 (2021).

25. Du, Y. P., Dalwani, M., Wylie, K., Claus, E. & Tregellas, J. R. Reducing susceptibility artifacts in fMRI using volume-selective *z* -shim compensation. *Magn. Reson. Med.* **57**, 396–404 (2007).

Main Figures

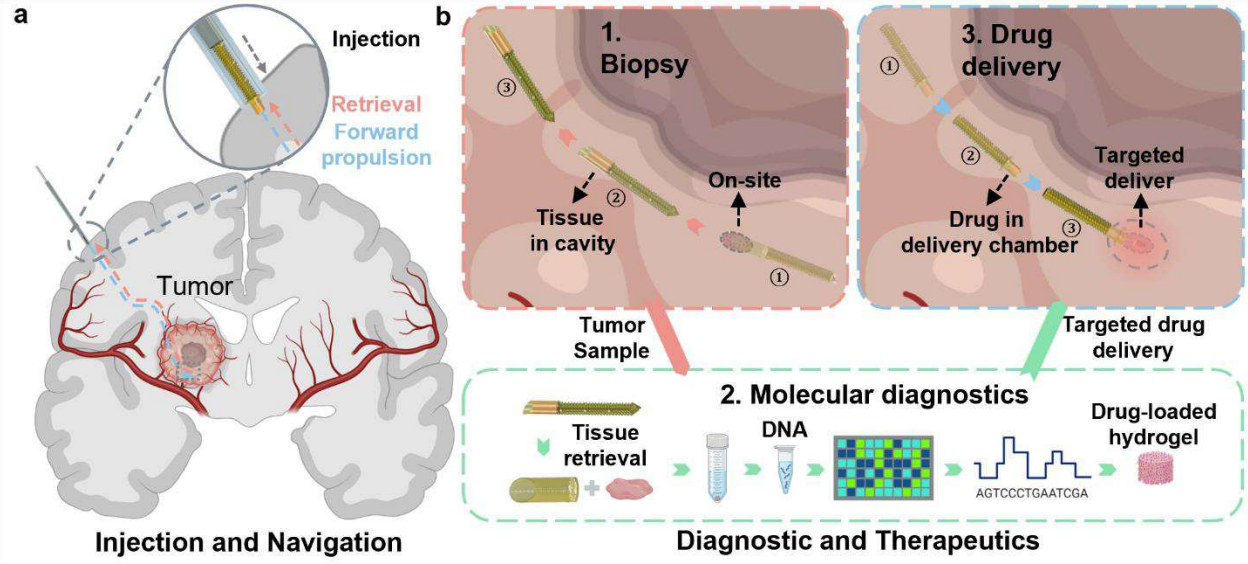


Fig. 1. BrainBot for wireless deep brain navigation. a. Schematic illustration of the BrainBot for biopsy and precise treatment of deep-seated brain tumors. **b**. Schematic overview of the three-step BrainBot workflow, including controlled 3D navigation to the deep-seated tumor and tissue biopsy with robot retrieval, molecular diagnostics of the biopsied tissue, and targeted drug delivery to the tumor with a second robot.

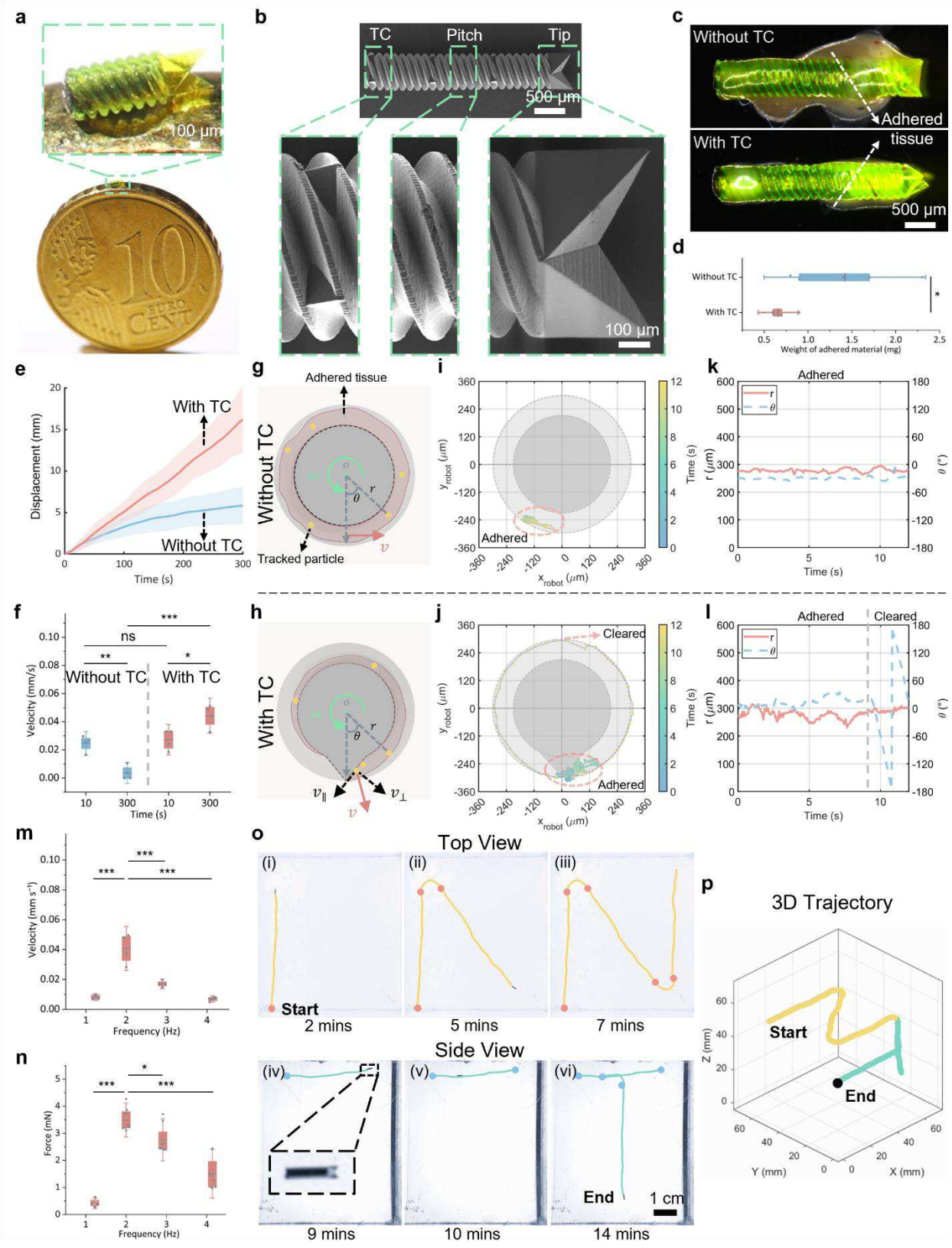


Fig. 2. BrainBot design and thread-clearing mechanism for enhanced penetration depth and load-carrying capability. a. Photograph of the BrainBot placed on a coin for size comparison. **b.** SEM images of the thread-clearing (TC), pitch, and tip structures. **c.** Representative images showing adhered brain tissue on the robot without and with TC. **d.** Comparison of the weights of the adhered materials on robots without and with TC. **e.**

Penetration depth of robots without and with TC over time. **f.** Propulsion velocities of robots without and with TC. **g-l**. particle tracking velocimetry (PTV) results of the thread models without and with TC on the upper and lower panel, respectively. The particle trajectories are displayed in the robot frame. **m.** Forward propulsion velocities in the porcine brain at different rotational frequencies. **n.** Propulsive forces at different rotational frequencies. **o.** Top and side views of the robot navigating in a transparent brain phantom along the planned trajectory of the letters 'N' and 'T' in different planes sequentially. **p.** Perspective view of the 3D trajectory of the robot. Error bars represent standard deviations. ns: not significant, * $p<0.05$, ** $p<0.01$, *** $p<0.001$.

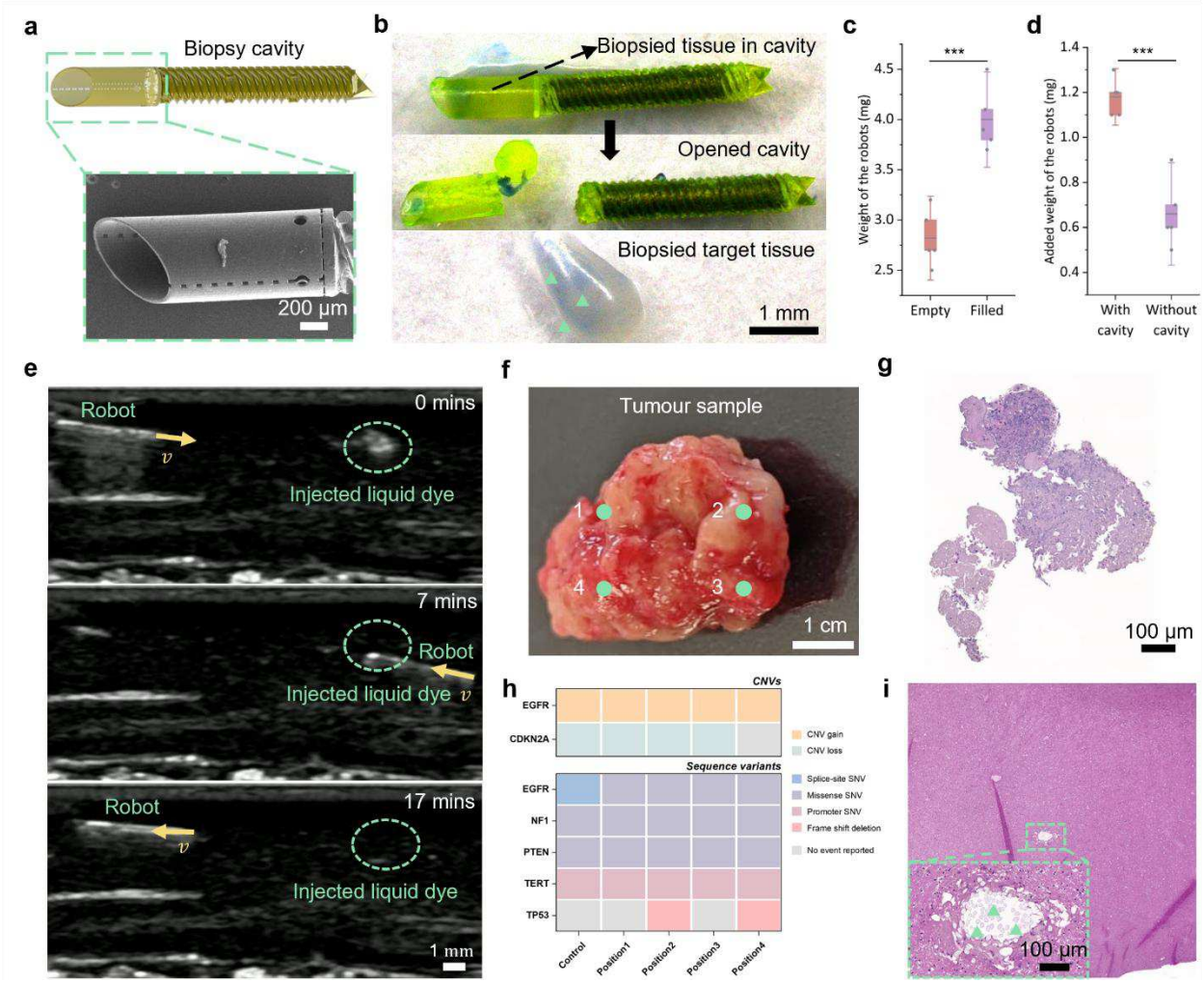


Fig. 3. Targeted tissue biopsy and tumor molecular diagnostics using the BrainBot. a. BrainBot design featuring a biopsy cavity at its trailing end. An SEM picture of the cavity structure. **b.** Representative images showing the BrainBot post-biopsy, the opened cavity for tissue release, and the retrieved tissue stained with methylene blue (green arrows). **c.** Weight of the robots before and after biopsy, showing a significant increase. **d.** Comparison of the added mass to robots. Robots featuring a cavity retrieved a significantly higher mass of tissue than cavity-free controls. **e.** Ultrasound image-guided biopsy procedure. Liquid dye was injected at the targeted site. Tissue collection was initiated at 7 min by reversing the robot's propulsion direction from forward to backward. **f.** Surgically resected patient tumor sample, with four marked target biopsy positions corresponding to four individual biopsy robots. **g.** Histological image of the biopsied sample collected by the robot. **h.** Genomic alterations at four sites comparing with the standard FFPE control sample. **i.** Histology images of porcine brain tissue after robot penetration. Green triangles in the inset mark cotton fibers carried by the robot as placeholders to prevent tissue collapse after the robot passing through. A minimal tissue defect with a diameter of 535 ± 59 μm was observed. Error bars represent standard deviations, *** $p<0.001$.

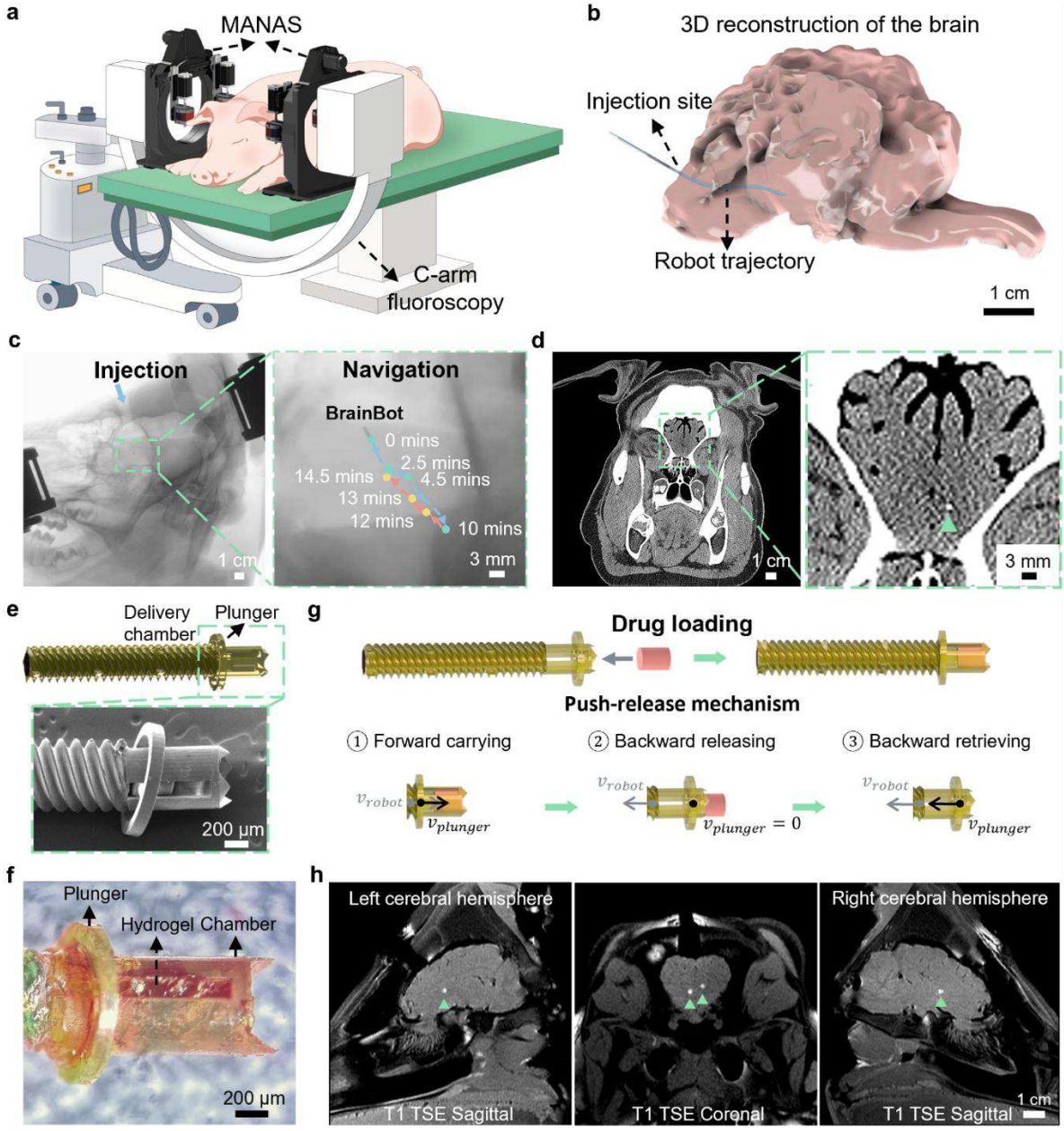


Fig. 4. Targeted drug delivery using the BrainBot to deep brain in an *ex vivo* porcine model. a. Schematic illustration of the BrainBot navigating in a porcine head under wireless magnetic actuation and clinical C-arm fluoroscopy guidance. **b.** CT reconstruction of the porcine brain showing the insertion point and the planned navigation trajectory of the robot. **c.** X-ray image of the porcine head positioned in the MANAS system. The enlarged overlaid X-ray image shows the forward and backward trajectory of the robot by tracking the endpoint of the onboard magnet. **d.** CT image showing the location of the robot after navigation (green arrow). **e.** BrainBot design featuring a drug delivery chamber at the front end. **f.** Photograph of the drug-loaded hydrogel inside the delivery chamber. **g.** Illustration of the targeted drug delivery mechanism. At the target site, the robot propels backward and the surrounding tissue holds the plunger stationary. This relative motion expels the drug-loaded hydrogel block. **h.** MRI images after two sequential deliveries (green arrows) to deep regions in the left and right hemispheres of the brain, respectively. A gadolinium-based contrast agent was used as the model drug. The absence of imaging artifacts confirms full retrieval of the magnetic robot.

Methods

Materials

Brain phantoms were prepared using 3% (w/v) gelatin (Type A, Sigma-Aldrich, Germany) in deionized water and solidified at 4 °C. All propulsion tests were conducted at room temperature. Load-carrying capacity was evaluated using copper wires (30 µm and 50 µm diameter; ELEKTRISOLA, Germany) and a polyamide optical fibre (250 µm diameter, efco creative GmbH, Germany). As the model drug, Gadovist (1.0 mmol mL^{-1}; Bayer AG, Germany) was combined with 20% (w/v) gelatin and incorporated into the drug chamber of the BrainBots.

Fabrication of robots

The BrainBots were fabricated using a two-photo lithography 3D printer (NanoOne with the UpPhoto resin, UpNano, Austria). Cylindrical neodymium rare earth magnets (diameter 0.38 mm, GMB Deutsche Magnetwerke, Germany) were embedded into the BrainBots post-printing. For the biopsy application, the biopsy unit was directly printed to the distal end of the BrainBot. For the load-carrying application, the selected cargo—such as copper microwire or optical fiber—was first bonded to the printed cap structure. This cap–cargo assembly was then inserted into the socket, and the complete unit was glued to the end of the BrainBot to ensure stable attachment during operation. For the drug delivery application, a drug cavity with a movable plunger was assembled to the front end of the BrainBot using an adhesive (LOCTITE 4902, Henkel AG & Co. KGaA, Germany).

Experiments on animal byproducts

No animals were euthanised for the purpose of this study. The porcine cadavers were used immediately post-mortem, following euthanasia carried out as part of separate, prior experiments conducted on the same day at the Experimental Operating Room of the NCT Dresden under approval number TVV 43/2023 (Saxon State Directorate). Because this work used only post-mortem tissue and involved no procedures on living animals, it required no separate animal-experiment approval. All animals were euthanised at the conclusion of prior procedures under deep anaesthesia with the intravenous injection of a lethal dose of potassium chloride, in accordance with the approved protocols. The porcine brains and heads were also obtained from the local butcher (Vorwerk Podemus e.K., Germany), and the experiments were carried out in 4-8 hours after sacrifice of the animals.

Experiments on *ex vivo* patient tumour samples

The BrainBots were tested for penetrating tumour samples removed from brain tumour patients. The study was approved by the University Hospital Carl Gustav Carus in Dresden, Germany (EK 323122008) and was conducted in accordance with the Declaration of Helsinki. Written informed consents were obtained from all participants. The resected tumour was kept in PBS buffer at 4°C. The penetration experiments were conducted within 2 hours after tumour removal.

Characterization of robots' propulsion

Robot designs with or without thread-clearing structures were evaluated for their ability to propel through brain tissue. Five design parameters of the robot were considered, namely, tip design, pitch, location of the TC structures, total length of the threads, and rotating frequency, to optimize for high propelling velocity and large thrust force. The optimized geometrical parameters are illustrated in Supplementary Fig. 8.

Robot propulsion in gel phantoms was imaged using a digital microscope (Dino-Lite Digital Microscope 3, DinoCapture, Netherlands) and tracked in MATLAB. Propulsion in *ex vivo* porcine brain were imaged using ultrasound imaging (Logiq P6; GE Healthcare Technologies, USA). Prior to testing, the pia mater was cut to make a small opening on the brain surface for robot insertion. The ultrasound gel was applied over the propulsion region to enhance acoustic coupling. For each robot design, the same procedure was repeated for 5 times independently. The ultrasound videos were analyzed using Tracker software (v.6.3.1, Open Source Physics, https://opensourcephysics.github.io/tracker-website/). Thrust forces were measured using a thin copper wire (50 μm) tethered between the load-carrying structure at the rear of the 3 mm-BrainBot and a force sensor (403A; Aurora Scientific, Canada).

PTV experiments

Two PTV experiments were carried out on customized optical systems to characterize the residue material clearing by the TC structure. Briefly, a laser beam (532 nm, 300 mW, LCX-532L-300, Oxxius, France) was spread by a Powell lens (LGL160, Thorlabs) for light sheet illumination.

In the first experiment, the threads of the BrainBot were pre-filled with gelatin (3% w/v) labelled with fluorescent particles (1 μm, F13082, Thermo Fisher Scientific Inc., USA) and then propelled through unlabelled gelatin. The propulsion was recorded using a digital camera (EOS, Canon, Japan) with a 5× objective and a long pass filter (OD4-550 nm, Edmund Optics, Barrington, USA). Particles adhering to the robot's surface were counted before and after propelling one body length to calculate percentage of cleared particles (Supplementary Fig. 3).

In the second experiment, a single thread model with or without TC (schematics in Supplementary Fig. 7) were rotated at around 0.41 Hz in the gelatin mixed with the same fluorescent particles as above. Videos were recorded by a customized microscope (Cerna, Thorlabs) with a 5× objective (MY5X-802B, Thorlabs Inc., USA) a filter cube (TLV-TE2000-TOM, Thorlabs Inc., USA) and a digital camera (Andor Solis ZYLA 4.2, Oxford Instruments, UK). The positions of the particles in the video were tracked using Tracker software and processed with MATLAB (R2024a, The MathWorks, USA). The results are presented in the robot frame in Fig. 2g-2l and Supplementary Fig. 4-5.

CFD simulation

CFD 3D simulations were performed in ANSYS Fluent R242 (ANSYS, Inc., Canonsburg, PA, USA). The fluid domain surrounding the device was a cylinder 1.2 mm in diameter and 4.625 mm in length, discretized with approximately 3.8×10^6 polyhedral cells for the case with TC and 3.2×10^6 polyhedral cells for the case without TC. Three inflation layers were implemented over the device and domain walls. A no-slip condition was imposed on all rigid walls, and the device surface was additionally assigned an angular frequency of 0.41 Hz. A laminar solver

with a pressure-velocity coupled scheme was used for the numerical solution. The fluid was modelled with a density of 1000 kg m^{-3}, and its rheology was described by a Herschel-Bulkley-Papanastasiou (HBP) model (Supplementary Fig. 6 and 7a).

Cell counting and DNA quantification for biopsy tissues

For cell isolation, the porcine brain tissues were carefully removed from the BrainBots and treated with Pierce™ neuron isolation enzyme (Thermo Fisher Scientific, USA) for 30 min according to the manufacturer's instruction. Cell counting was then performed with an automated cell counter (Countess 3, Thermo Fisher Scientific). To extract the DNA, porcine brain tissue samples were first submerged in 300 µL of DNA/RNA Shield (Zymo Research Corporation, USA) and homogenized. Then, each sample was added with 15 µL Proteinase K and 30 µL digestion buffer and incubated at room temperature for 30 min. DNA was then extracted using a ZYMO Quick-DNA/RNA Microprep Plus Kit (Zymo Research Corporation, USA) according to the manufacturer's instruction. The DNA was concentrated in 6 µL of elution, and the concentration was quantified using a UV-Vis spectrophotometer (NanoDrop One, Thermo Fisher Scientific).

Fluoroscopy, CT and MRI

The BrainBot was inserted into the grey matter of a porcine brain through a 9-mm burr hole in the skull and an opening on the dura matter. Of note, the size of the burr hole can be further minimized by using endoscopic cutting tools. Then, the BrainBot was actuated by MANAS and the navigation was recorded by fluoroscopy using a C-arm (Ziehm Vision RFD 3D, Ziehm Imaging, Germany). Sagittal projection images were acquired through the circular gantries of the MANAS at a frame rate of 1 fps. An orthopaedic fluoroscopy protocol with automatic exposure control was used at tube potentials ranging from 60 – 70 kVp.

Computed tomography (CT) was performed after the BrainBot reached the deep brain region. Images were acquired using a SOMATOM Definition Edge scanner (Siemens Healthineers, Erlangen, Germany) at a tube potential of 120 kVp and reconstructed into 0.8 mm slices using a sharp Hr60 kernel.

MRI was acquired on a 3T Biograph mMR PET/MRI (Siemens Healthineers, Erlangen, Germany). The porcine head did not fit into a human head coil. Instead, two flexible body coils were brought into a nearly cylindrical configuration to cover most of the head's perimeter. T1-weighted turbo spin echo imaging (TR/TE = 590/9.1 ms) was acquired with fat saturation in sagittal and coronal orientations and reconstructed into 2 mm image slices at an in-plane resolution of 0.74 mm. After the delivery of the model drug (MRI contrast agent) by BrainBot in the porcine brain, a subsequent T1-weighted turbo spin echo imaging was conducted to verify the successful delivery of the payload and the retrieval of the BrainBot (Fig. 4h).

3D reconstruction of CT

CT images were analyzed in 3D Slicer (v5.10.0, slicer.org). The reconstructed images were used to construct the 3D model with a slice thickness of 0.8 mm and an image matrix of 512 × 512 pixels in 3D Slicer. Semi-automatic segmentation was performed using the Segment Editor

module. Threshold-based segmentation was applied to delineate skin and bone structures. Manual refinement was conducted to remove segmented regions and to eliminate isolated small components. 3D surface models were generated from the segmented volumes using the built-in surface rendering algorithm. The reconstructed models were further processed using the Smoothing and Islands tools to reduce surface artifacts and remove disconnected small components. The final 3D surface models were exported in STL format for subsequent anatomical analysis and quantitative measurements.

Cytocompatibility of robots

Cell counting kit-8 (CCK-8) assay was applied to check the cytocompatibility of BrainBots. U-87 MG cells (a human glioblastoma cell line) were obtained from the American Type Culture Collection (ATCC, Manassas, USA) and regularly cultured in Dulbecco's Modified Eagle Medium (DMEM) supplemented with 10% of fetal bovine serum (FBS) and 1% penicillin-streptomycin under 5% CO_2 and 37 °C. To assess the cytocompatibility of BrainBots, U-87 MG cells were inoculated in a 96-well plate at the density of 8000/well in 100 μL of DMEM and cultured overnight, and then the medium in each well was replaced with fresh DMEM containing BrainBot (one for each well). After co-culturing for 24 h, the medium with BrainBot was discarded and FBS-free DMEM containing 10% CCK-8 solution (Proteintech Group, Germany) were added to each well and cultured for another 2 h. The absorbance of each well was then measured at the wavelength of 450 nm using a microplate reader (CLARIOstar Plus, BMG LABTECH, Ortenberg, Germany). Cells treated with PBS were used as blank control with cell viability as 100%. Meanwhile, a live/dead staining kit (Calcein AM/PI, Proteintech Group) was applied to stain the cells after co-culture with BrainBots, and cells were imaged using a fluorescent microscope (Leica DMi8, Wetzlar, Germany).

Histology procedures for the biopsy application

The patient tumour tissues biopsied by the BrainBot was collected and immediately fixed in 10% neutral buffered formalin for more than 24 h. The tumour tissues were embedded in paraffin, cut into 1-2 μm sections and stained with haematoxylin and eosin (H&E) stain. H&E-stained sections were digitized in brightfield mode using a Pannoramic SCAN 150 whole-slide scanner (3DHISTECH, Budapest, Hungary) equipped with a 20× Plan-Apochromat objective, yielding a spatial resolution of 0.204 μm per pixel. Digital slides were viewed using SlideViewer software (v2.8, 3DHISTECH). Histological analysis was performed by a board-certified pathologist.

Histology procedure for the assessment of tissue damage caused by BrainBot penetration

Due to the relaxation of the porcine brain tissue, the passages of the BrainBot were usually not easily found. A cotton wire (diameter ~400 μm) were attached to the rear of the BrainBot using the load-carrying mechanism. The GBM patient tumour in which the BrainBot penetrated was immediately fixed in 10% neutral buffered formalin for more than 24 h. The tumour was dehydrated, infiltrated, embedded in Technovit (Kulzer GmbH, Germany), polymerized, cut into 7 μm sections, and stained with H&E. The stained section was digitized in the same method mentioned above, and examined by an experienced pathologist. Quantitative analysis of the images was performed using MATLAB.

Statistical Methods

Each robot-testing trial was performed using a new robot. Adherent material mass and penetration depth were evaluated in five trials per robot design (Fig. 2d,e). Propulsion velocity was evaluated in four trials per design or rotational frequency (Fig. 2f,m), and propulsive force was evaluated in eight trials per rotational frequency (Fig. 2n). The experiments in Fig. 2e,f were performed using different porcine brains on different days, and the ones in Fig. 2m,n were performed using different porcine brains on the same day. The comparison of unloaded and tissue-loaded robot masses and the comparison of tissue mass collected by robots with and without a biopsy cavity each included five robots per group (Fig. 3c,d).

For experiments in 3% (w/v) gelatin phantoms, particle-clearing efficiency was evaluated in five trials per design (Supplementary Fig. 3c), rheological measurements were repeated three times (Supplementary Fig. 6a,b), and propulsion velocity and thrust force were evaluated in five trials per design (Supplementary Fig. 9a–f). In porcine brain tissue, propulsion velocity was evaluated in three trials per design using different porcine brains on the same day (Supplementary Fig. 10a–c). Minimum turning radius and collected tissue mass were evaluated in three and five trials per design, respectively (Supplementary Figs. 11 and 15c). Cell and DNA concentrations were measured in nine and twelve repeats, respectively (Supplementary Fig. 16a,b). Tissue damage sizes and area were each quantified from 22 measurements and summarized as mean ± s.d. (Supplementary Fig. 20a,b).

Two-group comparisons were performed using two sample t-tests (Welch's). These comparisons included adherent material mass (Fig. 2d), unloaded versus tissue-loaded robot mass (Fig. 3c), tissue mass collected by robots with versus without a biopsy cavity (Fig. 3d and Supplementary Fig. 15c), particle-clearing efficiency (Supplementary Fig. 3c) and minimum turning radius (Supplementary Fig. 11). Comparisons across designs or operating conditions in Fig. 2f,m,n and Supplementary Figs. 9a–f and 10a–c were performed using one-way analysis of variance (ANOVA) followed by Tukey's multiple-comparison test for pairwise comparisons. Penetration-depth trajectories, rheological measurements, cell and DNA concentrations, and tissue damage measurements were summarized descriptively.

Statistical analyses were performed using OriginPro 2024 (OriginLab Corporation, USA). Statistical significance was defined as $p < 0.05$, using multiplicity-adjusted P values for Tukey's comparisons. Where indicated, significance levels are denoted by $*p < 0.05$, $**p < 0.01$ and $***p < 0.001$; NS denotes not significant.

Data availability

The authors declare that all data that support the findings of this study are provided in the main text and Supplementary Information.

Code availability

Requests for custom codes should be addressed to Tian Qiu.

Acknowledgements

This work was partially funded by the European Union (ERC, VIBEBOT, 101041975), the Helmholtz Biomedical Engineering Initiative (RoboT^3), the German Cancer Research Centre (DKFZ), the DKFZ-MOST cooperation program (Ca 221), the German Research Foundation

(DFG) EXC 2050/2 (CeTI, 390696704). J.T. thanks the Marie Skłodowska-Curie Fellowship (HyBOT, 101209455). Y.G. thanks the Alexander von Humboldt Foundation. We thank the imaging platform at NCT Dresden; S. Herold and M. Meinhardt (Department of Pathology) for performing next-generation sequencing and interpreting histological images; and S. Manthey, A. Wenke and S. Schulze (University Centre of Orthopaedics, Trauma and Plastic Surgery, University Hospital Dresden) for preparing histological sections.

Author contributions

T.Q. conceived and supervised the study, with clinical input and guidance from T.J. M.Z., J.K.M., and M.J. led the experimental design of the study, designed and fabricated the robots, and conducted robot testing in *ex vivo* brain tissue and gel phantom models. M.J. developed the MANAS. M.Z., J.K.M., M.J., A.N.J.S., J.T., R.A., R.Y., M.W., T.J., and T.Q. performed postmortem porcine experiments. R.A. performed CT and MRI. Y.G. conducted the cytocompatibility assays and post-biopsy analyses. A.N.J.S. carried out histology analysis. H.W., and L.T. contributed to the characterization and optimization of the robots. A.M. contributed to the data acquisition and analysis of the ultrasound videos. T.M., N.K., K.I.M., A.L. performed CFD simulation and theoretical modelling. All authors contributed to data analysis, writing, editing and review of the manuscript.

Use of artificial intelligence

During the preparation of this manuscript, the authors used ChatGPT / Gemini developed by OpenAI / Google to assist with the language polishing to improve overall readability. After using these tools, the authors reviewed and edited the content as necessary and take full responsibility for the final content of the publication.

Competing interest declaration

M. Zhang and T. Qiu have a pending patent on the device for propulsion in viscoelastic materials (EP25202803). The other authors declare no competing interests.

Additional information

Correspondence and requests for materials should be addressed to Tian Qiu.

Supplementary Files

This is a list of supplementary files associated with this preprint. Click to download.

- SIVideo1BrainBotpropellinginthebrainphantom.mp4
- SIVideo3CorotationoftheadheredmaterialontherobotwithoutTC.mp4
- SIVideo11CargotransportationanddeploymentmechanismofthemicrowireSI.mp4
- SIVideo12BrainBottransportingamicrowireinphantomandporcinebrain.mp4
- SIVideo9BrainBotsteeringtobypassanobstacleunderultrasoundguidance.mp4
- SIVideo6Penetrationofentireporcinebrain.mp4
- SIVideo13Fluoroscopyguidednavigationinporcinehead.mp4
- SIVideo7Ultrasoundguidednavigationinporcinehead.mp4
- SIVideo10Ultrasoundguidedtransportationofanopticalfibrethroughporcinebrain.mp4
- SIVideo2ThreadclearingeffectivenessoftheTCstructure.mp4
- SIVideo14Ultrasoundguideddrugdeliveryinporcinebrain.mp4
- SITextv5.docx
- SIVideo8Ultrasoundguidedbiopsyinporcinebrain.mp4
- SIVideo53DpropulsiontrajectoryoftherobotinthebrainphantomSI.mp4
- SIVideo4ClearanceoftheadheredmaterialontherobotbyTC.mp4